Sound & Vibration 2025, 59(5), 3701.
doi: https://doi.org/10.59400/sv3701

Article

Analysis and control of 2f noise in an ultra-high-speed permanent magnet synchronous motor

Guoping Feng[1,*], Ruihong Jing[1], Jing Yao[2], Jianjun Zhao[2,*], Dongya Li[3], Wenjian Zhou[4]

[1] School of Intelligent Manufacturing, Suzhou Chien-Shiung Institute of Technology, Suzhou 215000, China
[2] State Key Laboratory of Intelligent Optimized Manufacturing in Mining & Metallurgy Process, Beijing 100089, China
[3] Applied Technology College, Soochow University, Suzhou 215000, China
[4] College of Power and Energy Engineering, Harbin University of Science and Technology, Harbin 150006, China
*** Corresponding author:** Guoping Feng, fgpatsd@163.com; Jianjun Zhao, zhao_jj@bgrimm.com

CITATION

Feng G, Jing R, Yao J, et al. Analysis and control of 2f noise in an ultra-high-speed permanent magnet synchronous motor. Sound & Vibration. 2025; 59(5): 3701. https://doi.org/10.59400/sv3701

ARTICLE INFO

Received: 10 September 2025
Revised: 28 September 2025
Accepted: 5 October 2025
Available online: 28 October 2025

Abstract: Ultra-high-speed permanent magnet synchronous motors (PMSMs) have been widely applied in aerospace, advanced manufacturing, and consumer products due to their small size, high reliability, and high-power density. As the rotational speed increases, losses, cooling requirements, excitation forces, bearing losses, and noise characteristics of the motor are significantly different from those of conventional motors. To minimize iron losses and improve efficiency, ultra-high-speed motors typically employ a low pole count configuration, exemplified by the prevalent 2-pole 3-slot (2P3S) design. In 2-pole machines, low-order electromagnetic excitation forces may cause significant electromagnetic vibration and noise. Reducing electromagnetic noise, especially the two-times mechanical rotational frequency (2f) noise in 2P3S motors, is critical. Therefore, the noise reduction strategies for a 120,000 rpm PMSM are investigated. First, the electromagnetic excitation frequencies and magnitudes of the motor are analyzed. Through changing the pole-slot configuration (such as transitioning from 2P3S to 2P6S), the unbalanced magnetic pull (UMP) in the original 2P3S design is eliminated, significantly reducing the main source of vibration. Then, the impact of the stator assembly gap on electromagnetic excitation is examined using a segmented stator structure. Effective control of this assembly gap further reduces the electromagnetic noise of the motor. Finally, experimental tests demonstrate a significant noise reduction in the 2f frequency band, with a sound pressure level reduction of about 9 dB. The reduction validates the effectiveness of this pole-slot optimization and stator assembly gap control strategies.

Keywords: ultra-high-speed; permanent magnet synchronous motor; unbalanced magnetic pull; noise; assembly gap

1. Introduction

Ultra-high-speed motors (exceeding 100,000 rpm) are typically designed as PMSMs due to their compact size, high efficiency, and robust reliability. Ultra-high-speed PMSMs are widely applied in aerospace, high-end manufacturing, and household appliances. In the operation of ultra-high-speed motors, noise has become an increasing concern for manufacturers and users. As rotational speed increases, the noise issue becomes more significant than in low-speed motors. Effectively reducing the noise of ultra-high-speed motors is crucial for their development and application.

The noise generated by ultra-high-speed permanent-magnet motors has been studied worldwide. Gao et al. [1] established an electromagnetic-structural-acoustic multiphysics coupling model for a 150,000 rpm ultra-high-speed PMSM. They focused on structural vibration and noise caused by electromagnetic force waves, and achieved effective vibration and noise suppression by optimizing the rotor sleeve material and stator modal properties. Wang et al. [2] provided a comprehensive review of active vibration control methods for high-speed PMSMs, including voltage injection techniques to counteract specific electromagnetic excitation forces. Active control can be used as an effective supplementary means for suppressing broadband vibration in high-speed motors. Liu et al. [3] analyzed electromagnetic vibration in a high-speed motor, and innovatively considered the flexibility of the stator core and the effect of the housing. They found that traditional rigid assumptions overestimate the natural frequencies of the structure. A flexible model can predict mid-to-high frequency vibration responses more accurately, providing a new perspective for precise NVH design. Peng et al. [4] investigated a 150,000 rpm compressor motor supported by magnetic bearings, with a focus on rotor dynamics and vibration reduction. The magnetic bearings can provide active damping to suppress vibrations when passing through critical speeds, and compensate in real time for unbalanced magnetic forces. These studies focus on noise reduction through the pathway of structural vibration transmission. While vibration path control methods are valuable, their applicability to ultra-high-speed motors is limited, as they do not directly address the source of excitation. Specifically, these methods primarily concentrate on controlling the transmission of structural vibrations rather than mitigating the electromagnetic forces that generate the noise. The lack of direct engagement with electromagnetic noise sources, especially at higher speeds, means that these methods are unable to fully address the fundamental causes of noise in ultra-high-speed motors.

Conversely, many researchers strive to reduce motor vibration and noise during the electromagnetic design phase by minimizing cogging torque and torque ripple. Yi et al. [5] applied a multi-objective genetic algorithm to optimize a 150,000 rpm motor. They also optimized the magnet shape, pole arc coefficient, and air gap length to minimize the cogging torque, torque ripple, and maximize efficiency, achieving an optimal balance between low vibration and high performance. Bianchi et al. [6] systematically analyzed the causes of cogging torque in surface-mounted PMSMs and proposed methods such as optimizing magnet pole arc width and stator slot opening to effectively suppress cogging torque. This work provides an important theoretical basis for subsequent low-noise motor design. Zhu et al. [7] discussed the influence of several key design parameters on cogging torque. The findings were validated through analytical and numerical methods. Jahns et al. [8] reviewed the techniques for minimizing pulsating torque (including cogging torque and torque ripple) in permanent-magnet AC drives, including motor design optimizations and control strategy approaches. Islam et al. [9] focused on reducing cogging torque in mass-produced BLDC motors and proposed a practical solution that specially considers manufacturing tolerances. Wang et al. [10] compared different pole-slot combinations and electromagnetic performance metrics (including torque ripple and noise), providing

an important reference for high-speed BLDC motor design. Anuja and Doss [11] used magnet segmentation and circumferential shifting technology to eliminate cogging torque, significantly reducing torque ripple and associated force harmonics in a BLDC motor. Huang and Feng expanded the scope from electromagnetic noise to include mechanical and aerodynamic noise in high-speed motors. Huang et al. [12] showed that once the rotational speed exceeds a certain threshold, high-speed friction between the rotor surface and air generates significant aerodynamic noise. This noise is generally broadband, and its sound pressure level increases exponentially with rotational speed. They found that improving the surface smoothness of the structure, or applying special coatings are effective means of reducing aerodynamic noise. At ultra-high rotational speed, aerodynamic effects become particularly pronounced. Minute manufacturing tolerances and eccentric loading at the air inlet can induce significant eddy generation. These eddy currents subsequently contribute to an augmentation in mechanical structural vibrations. As a result, the eccentricity of the motor shaft increases, along with misalignment between the stator and rotor, leading to a notable rise in both mechanical and electromagnetic noise levels. Feng et al. [13] proposed a noise reduction method for the coupling of first-order aerodynamic and mechanical noise in high-speed motors. These studies improve performance by considering aerodynamic effects and coupling them with electromagnetic forces. However, this method is challenging to implement in practical high-speed motor designs, as it requires significant computational effort to model wide-frequency responses.

For ultra-high-speed PMSMs exceeding 100,000 rpm, the electromagnetic excitation frequencies are exceedingly high, often reaching several kHz. These high-frequency excitations can easily couple with the mid-to-high order vibration modes of the lightweight and flexible stator structure, leading to severe vibrations and audible noise. Compared with low-speed motors, addressing the noise, vibration, and harshness (NVH) in ultra-high-speed motors requires tracing back to the spatiotemporal force waves generated in the air gap, which constitute the basic physical source of excitation. Current work mainly focuses on traditional vibration path control methods and the suppression of cogging torque and torque ripple. However, the NVH issues of ultra-high-speed PMSMs require precise control of specific spatial orders and time-frequency components of radial electromagnetic force waves. In addition, electromagnetic noise in ultra-high-speed motors is not caused by a single factor such as cogging torque or torque ripple; on the contrary, it is usually caused by the coupling of cogging torque, radial electromagnetic forces, and mechanical excitations. Therefore, to effectively control vibration noise, it is necessary to eliminate the critical low-order radial electromagnetic force waves and cogging torque at the same time [14–20]. This requires identifying key force wave frequencies and spatial harmonics from the air-gap field, and then weakening their main components at the source through targeted measures. Innovative pole-slot combination designs [21–24], magnetic circuit topology optimization, multi-objective coupling design based on intelligent algorithms [25, 26], and active electromagnetic force compensation have become the cutting-edge and core strategies for fundamentally suppressing vibration noise from the perspective of electromagnetic design.

In response to this, we first calculate the electromagnetic forces acting on the inner surface of the stator in an ultra-high-speed 2P3S motor. Then the main excitation frequency components and spatial force waves are analyzed. To alleviate low-order spatial force waves, especially those with 2f frequency, the pole-slot combination is optimized, leading to the development of a 2P6S optimization scheme. Taking into account the segmented stator assembly structure of the motor, the impact of the assembly gap on low-order electromagnetic noise is discussed. Finally, a combined strategy combining pole-slot configuration and segmented stator gap control is used to verify the results of noise reduction.

2. Materials and methods

A 2-pole 3-slot (2P3S) ultra-high-speed PMSM is studied. The rated speed of the motor is 120,000 rpm, and the designed power is 450 W. The system consists of a stator core, rotor assembly (rotor core and impeller), and an intake and duct system.

According to the theory of vibration and noise, noise reduction requires establishing a coupled vibration equation between the motor structure and acoustic field [27]. By discretizing this coupled equation, one can obtain the displacement or acceleration responses on the surface of the structure can be obtained by discretizing this coupled equation. In addition, using the acoustic wave equation, the Helmholtz integral equation of sound pressure can be solved using the boundary element method to obtain the normal displacement or velocity of points on the structural surface and the sound pressure gradient, thereby obtaining the sound pressure in the field. In ultra-high-speed motors, noise can be reduced by applying sound absorption/isolation along the transmission path or by reducing the excitation at the source. In this work, the noise generation mechanism is focused on, and the excitation sources are analyzed to reduce the excitation loads at the source. Based on the excitation of the motor, two load conditions are concentrated on loads that have a significant influence on 2f noise: the electromagnetic excitation load and the eccentric excitation caused by rotor-stator misalignment.

2.1. Analysis of electromagnetic excitation force

In a PMSM, using the Maxwell stress tensor method, the radial and tangential force waves per unit area on the inner surface of the stator core (causing electromagnetic noise) are proportional to the square of the air-gap flux density, that is:

$$f_r = \frac{1}{2\mu_0}\left(B_r^2 - B_t^2\right), \quad f_t = \frac{1}{\mu_0} B_r B_t, \tag{1}$$

where B_r is the radial air-gap flux density; B_t is the tangential air-gap flux density; $f_r(\theta,t)$ is the radial electromagnetic force wave density, $f_t(\theta,t)$ is the tangential electromagnetic force wave density, and μ_0 is the permeability of vacuum. B_x and B_y are the components of the air-gap flux density along the axes, and θ is the relative position angle of the stator and rotor.

In a PMSM, the air-gap field comprises the field generated by the permanent magnets and the armature field generated by the windings carrying current. Both

are rotating fields with spatial distribution and time-varying characteristics. The stator slotting only affects the spatial distribution of the air-gap field, and the relative permeance of the air-gap is typically introduced to explain the slotting. The magnetic flux density of the permanent magnet and the magnetic flux density of the armature are linearly superimposed, and then multiplied by the relative magnetic permeability of the air gap:

$$B_r = (b_{rm}+b_{ra})\,\lambda_a \tag{2}$$

where b_{rm}, b_{ra}, and λ_a represent the radial permanent magnet flux density, radial armature flux density, and air-gap relative permeance, respectively. They can be expressed as Fourier series:

$$\begin{aligned} b_{rm} &= \sum_{n\,=\,1,3,5,\ldots}^{\infty} b_{m,n}\cos\left(np\theta - n\omega t\right), \\ b_{ra} &= \sum_{\nu\,=\,1,5,7,\ldots}^{\infty} b_{\nu}\cos\left(\nu p\theta - \omega t - \phi\right), \\ \lambda_a &= \lambda_{a0} + \sum_{\mu=1}^{\infty} \lambda_{a,\mu}\cos\left(\mu Q_s\theta\right). \end{aligned} \tag{3}$$

where θ is the spatial angle; t is time; p is the pole pair number; Q_s is the number of stator slots, and ω is the motor angular speed. $b_{m,n}$, b_{ν}, and $\lambda_{a,\mu}$ are the harmonic amplitudes of the permanent magnet flux density, armature flux density, and relative permeance, respectively.

The radial force waves in a motor can be represented as a superposition of force waves with different spatial orders and frequencies:

$$\begin{aligned} f_r &= \left[\frac{1}{2\mu_0}\left(\sum_{n=1,3,5,\ldots}^{\infty} b_{m,n}\cos\left(np\theta - n\omega t\right) + \sum_{\nu=1,5,7,\ldots}^{\infty} b_{\nu}\cos\left(\nu p\theta - \omega t - \phi\right)\right) \times \left(\lambda_{a0} + \sum_{\mu=1}^{\infty}\lambda_{a,\mu}\cos\left(\mu Q_S\theta\right)\right)\right]^2 \\ &= \frac{1}{4\mu_0^2}\left\{\sum_{n_1}\sum_{n_2} b_{m,n1}b_{m,n2}\left\{\cos\left[\left(n_1 \pm n_2\right)p\theta - \left(n_1 \pm n_2\right)\omega t\right]\right\} + 2\sum_{n}\sum_{\nu} b_{m,n}b_{\nu}\left\{\cos\left[\left(n \pm \nu\right)p\theta - \left(n \pm 1\right)\omega t \pm \phi\right]\right\}\right. \\ &\quad + \sum_{\nu_1}\sum_{\nu_2} b_{\nu_1}b_{\nu_2}\left\{\cos\left[\left(\nu_1+\nu_2\right)p\theta - 2\omega t - 2\phi\right] + \cos\left[\left(\nu_1-\nu_2\right)p\theta\right]\right\} \times \\ &\quad \left.\left\{\lambda_{a0}^2 + 2\lambda_{a0}\sum_{\mu}\lambda_{a\mu}b_{\nu}\cos\left(\mu Q_S\theta\right) + \sum_{\mu_1}\sum_{\mu_2}\lambda_{a,\mu1}\lambda_{a,\mu2}\cos\left[\left(\mu_1 \pm \mu_2\right)Q_S\theta\right]\right\}\right\} \end{aligned} \tag{4}$$

According to Equation (4), under ideal conditions, the frequency component of the radial force wave is an even multiple of the fundamental current frequency, that is, an integer multiple of the pole-passing frequency. The term ($n_1 \pm n_2$) represents the radial force waves generated by the interaction between different harmonic components of the permanent magnet magnetic fields. ($n \pm 1$) denotes the radial forces generated by the

interaction between the permanent and the armature magnetic fields. 2f represents the radial forces generated by the armature magnetic field. For ultra-high-speed motors, a small pole number (typically a 2-pole design) is generally selected to improve electromagnetic efficiency and reduce losses. The frequencies of radial electromagnetic force waves are 2f, 4f, 6f, and more. According to Equation (4), a 2f electromagnetic force wave is usually generated by the interaction between the fundamental field of the permanent magnets and the windings. Compared with harmonic fields, the fundamental field has the largest flux density amplitude; that is, the fundamental components in each term are the largest. Therefore, the radial electromagnetic force at 2f is the strongest, and the noise is the most significant. Moreover, 2f is the lowest frequency and the most easily excited structural mode of the motor. From this perspective, improving the 2f noise of ultra-high-speed PMSMs is crucial.

2.2. Influence of pole-slot combination

Zhu et al. and Chen et al. [28, 29] simplified the motor structure to a cylinder and derived the relationship between the stator deformation and the spatial order of electromagnetic force waves (considering only stator circumferential modes) based on vibration noise theory. It showed that the deformation of the stator structure is inversely proportional to the fourth power of the spatial order of the radial force wave. Therefore, when calculating the radiated noise of a motor, attention can be paid to low-order spatial force harmonics (with large amplitudes), and higher-order ones can be neglected. Based on this, for the 2P3S motor with a 2f frequency, low-order spatial force waves ($r < 4$) are: (1) an $r = 2$ force wave generated by the fundamental magnetic flux; and (2) an $r = -1$ force wave generated by the interaction between the magnetic field of the motor and the stator tooth harmonic, where $r = -1$ corresponds to an UMP. The $r = -1$ force wave in the 2P3S motor can cause severe electromagnetic noise at 2f; this excitation should be eliminated first.

To improve electromagnetic noise at 2f and eliminate the UMP in the 2P3S motor, it is necessary to change the number of the stator slot Q_s according to Equation (4). Although the 2P6S configuration is selected based on the condition that gcd ($2p$, Q_s) > 1, other configurations, such as 2P9S, can also be considered. An increase in Q_s can refines the magnetic field distribution, enabling the air-gap magnetic field to more closely approximate a sinusoidal waveform and reducing harmonic content. As a result, iron loss usually shows a downward trend, thereby improving motor efficiency. On the other hand, an increase in the slot number will lead to high complexity of winding configuration and increased manufacturing costs, especially in the ultra-high-speed compact motors. The 2P6S configuration achieves a balance between various factors and makes it a suitable choice for this study. **Figures 1** and **2** show the stator and rotor designs of the two pole-slot combinations under the same requirements, respectively.

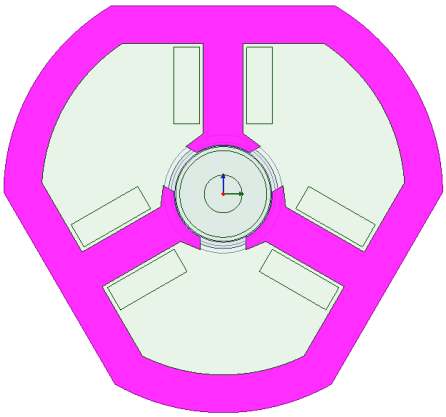

Figure 1. Stator and rotor scheme of a 2P3S motor.

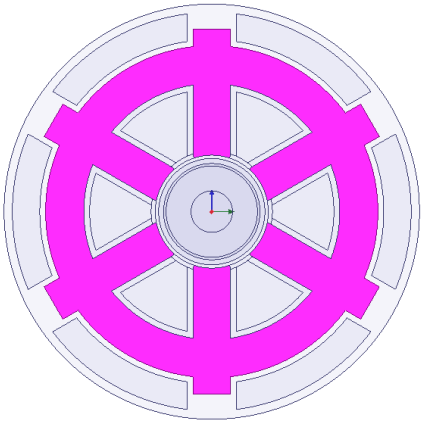

Figure 2. Stator and rotor scheme of a 2P6S motor.

2.3. Influence of segmented stator assembly gap

In the optimized 2P6S motor, a segmented stator structure is adopted to improve the manufacturability and influence the vibration characteristics. The stator is divided into two halves and assembled together to form a complete core, as shown in **Figures 3** and **4**. The two stator halves are connected through matching keys and slots on the interface. Due to manufacturing tolerances and inaccurate assembly, there is inevitably a small gap between the two stator core halves.

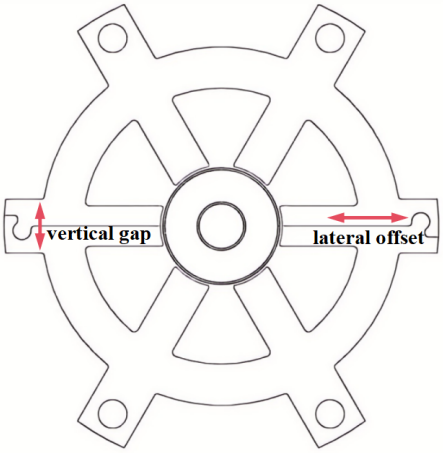

Figure 3. Schematic diagram of the 2P6S motor segmented stator assembly and gap.

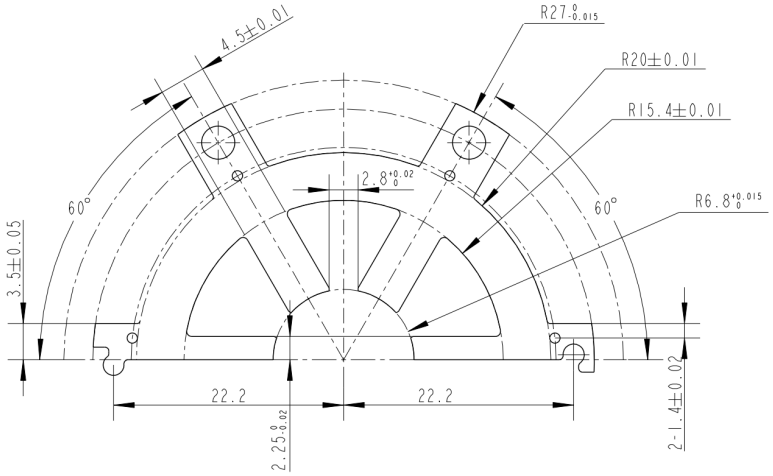

Figure 4. Engineering drawing of the segmented stator laminations.

This stator assembly gap has two components: a lateral offset (lateral misalignment of the halves along the joining plane) and a vertical gap (a slight separation or opening of the interface). **Figure 3** labels these as the lateral offset and the vertical gap between the stator segments. An assembly gap means that the stator and rotor are no longer completely concentric, thereby introducing rotor eccentricity (which can be static or dynamic depending on whether the misalignment is fixed or changing with rotation). Considering the manufacturability of stator segmented assembly, process precision, and the economic efficiency of production, the acceptable limits for lateral offset and vertical gap should not exceed 0.05 mm. Both vertical gap and lateral offset fall in the range of [0.01 mm, 0.05 mm]. According to electromagnetic theory, even a small eccentricity can disrupt the distribution of the air-gap flux. The eccentricity between rotor and stator generates additional air-gap field harmonics with pole counts of $p \pm 1$, $v \pm 1$, $\mu \pm 1$. When these harmonics interact with the fundamental field, new radial force waves will be generated. Deriving the expressions of the radial force under static and dynamic eccentricity (represented by Equations (6) and (7)),

$$f_r = \frac{1}{4\mu_0^2}\sum_{r,j} B_{r,j}\cos\left(r\theta + s_{r,\omega}\omega_{r,j}t + \varphi_{r,j}\right)\left(1+\varepsilon\cos\left(\theta\right)\right)^2$$

$$= \frac{1}{4\mu_0^2}\sum_{r,j} B_{r,j}\cos\left(r\theta - s_{r,\omega}\omega_{r,j}t + \varphi_{r,j}\right) + \frac{\varepsilon^2}{8\mu_0^2}\sum_{r,j} B_{r,j}\cos\left(r\theta - s_{r,\omega}\omega_{r,j}t + \varphi_{r,j}\right) +$$

$$\frac{\varepsilon}{4\mu_0^2}\sum_{r,j} B_{r,j}\left\{\begin{array}{c}\cos\left[(r+1)\,\theta - s_{r,\omega}\omega_{r,j}t + \varphi_{r,j}\right] \\ +\cos\left[(r-1)\,\theta - s_{r,\omega}\omega_{r,j}t + \varphi_{r,j}\right]\end{array}\right\} +$$

$$\frac{\varepsilon^2}{16\mu_0^2}\sum_{r,j} B_{r,j}\left\{\begin{array}{c}\cos\left[(r+1)\theta - s_{r,\omega}\omega_{r,j}t + \varphi_{r,j}\right] \\ +\cos\left[(r-1)\theta - s_{r,\omega}\omega_{r,j}t + \varphi_{r,j}\right]\end{array}\right\} \tag{6}$$

$$f_r=\frac{1}{4\mu_0^2}\sum_{r,j}B_{r,j}\cos\left(r\theta+s_{r,\omega}\omega_{r,j}t+\varphi_{r,j}\right)\left(1+\varepsilon\cos\left(\theta-\omega_r t\right)\right)^2$$

$$=\frac{1}{4\mu_0^2}\sum_{r,j}B_{r,j}\cos\left(r\theta-s_{r,\omega}\omega_{r,j}t+\varphi_{r,j}\right)+\frac{\varepsilon^2}{8\mu_0^2}\sum_{r,j}B_{r,j}\cos\left(r\theta-s_{r,\omega}\omega_{r,j}t+\varphi_{r,j}\right)+$$

$$\frac{\varepsilon}{4\mu_0^2}\sum_{r,j}B_{r,j}\left\{\begin{array}{l}\cos\left[(r+1)\,\theta-(s_{r,\omega}\omega_{r,j}+\omega)t+\varphi_{r,j}\right]\\+\cos\left[(r-1)\,\theta-(s_{r,\omega}\omega_{r,j}-\omega)t+\varphi_{r,j}\right]\end{array}\right\}+ \tag{7}$$

$$\frac{\varepsilon^2}{16\mu_0^2}\sum_{r,j}B_{r,j}\left\{\begin{array}{l}\cos\left[(r+2)\,\theta-(s_{r,\omega}\omega_{r,j}+2\omega)t+\varphi_{r,j}\right]\\+\cos\left[(r-2)\,\theta-(s_{r,\omega}\omega_{r,j}-2\omega)t+\varphi_{r,j}\right]\end{array}\right\}$$

It is found that the main resulting force wave has a spatial order of $r = p \pm 1 - p = \pm 1$, which is also a UMP. It is crucial that this eccentricity-induced UMP oscillates at the two-times rotational frequency (2f). In other words, even in a symmetrical 2P6S design, any assembly gap that causes rotor eccentricity will reintroduce a 2f radial force component. Thus, controlling the assembly gap is necessary to prevent the generation of new 2f electromagnetic excitations. In this method, to minimize the lateral offset and vertical gap between stator halves through precision machining and assembly control, the influence of different gap sizes on the electromagnetic forces and resulting noise is analyzed.

3. Electromagnetic excitation simulation analysis

3.1. Electromagnetic analysis of 2P3S and 2P6S

Both motor schemes described above use finite element analysis (FEA) to simulate their electromagnetic excitation forces. These simulations are conducted under rated operating of the motor. **Table 1** shows the key simulation parameters and the performance at the same speed of 120,000 rpm. To ensure fair comparison, the phase winding and current in the triangular connection are adjusted, so that both motors produce almost the same output torque and power, about 48 mN·m and 430 W respectively. The performance of the 2P6S motor is comparable to that of the 2P3S motor, indicating that the proposed pole-slot combinations will not damage the basic electromagnetic performance.

Table 1. Parameters and performance of finite element simulation.

Motor design	Winding current (A, △-connected)	Speed (rpm)	Torque (mN·m)	Output power (W)
2P3S (original)	18.50	120,000	47.82	425
2P6S (optimized)	18.26	120,000	49.68	432

Note: △-connected refers to a three-phase winding or load connection in which the phase windings are connected to form a closed triangular loop.

The magnetic flux density distribution and the radial electromagnetic forces are calculated for each design. **Figures 5** and **6** show the magnetic field line distribution of 2P3S and 2P6S motors at rated speed, respectively. The maximum flux per unit length of the flux lines is basically the same, 0.0052 Wb/m. Importantly, the 2P6S motor has a

symmetric stator-rotor magnetic circuit with evenly distributed flux lines. However, the magnetic circuit of 2P3S is clearly asymmetric, which can easily lead to severe UMP.

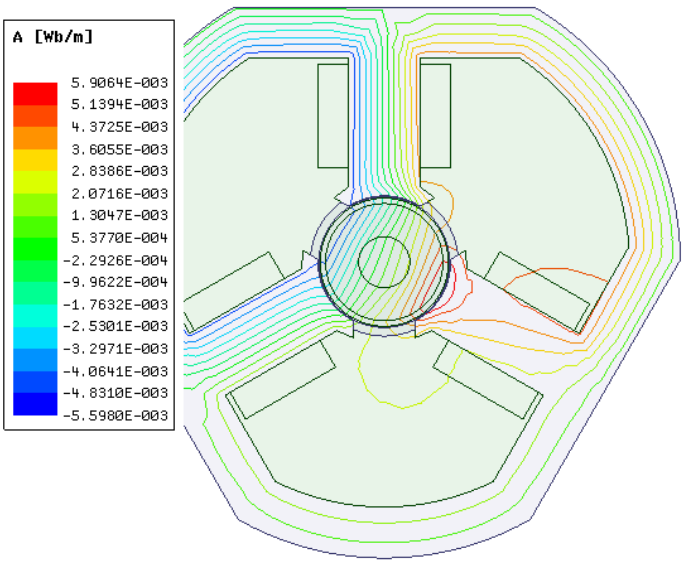

Figure 5. Magnetic field lines of the 2P3S motor.

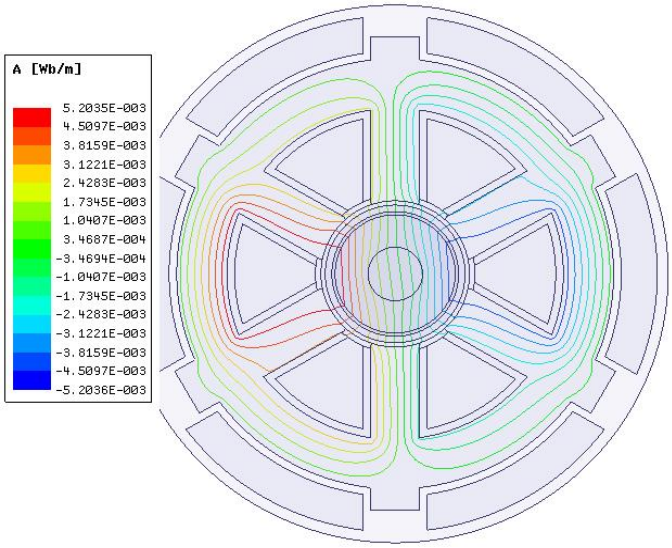

Figure 6. Magnetic field lines of the 2P6S motor.

Figure 7 shows the forces on the rotor in the X and Y directions after one rotation under load. The UMP of the 2P3S motor is about 12 N, imposing a significant one-sided radial load on the shaft and bearings of the motor and adversely affecting the operation. In contrast, the 2P6S motor with a symmetric stator-rotor magnetic circuit and uniform flux distribution does not have UMP. This difference accounts for the fundamental pole-slot combinations in the design.

The excitation is decomposed into radial forces, as shown in **Figure 8**. The 2P3S motor experiences a large alternating radial force at 2f, with a unilateral amplitude of about 12 N (with a peak-to-peak value of 24N). Such a large 2f radial force will inevitably affect the noise of the motor, especially when it is coupled with mechanical excitations of the stator and rotor.

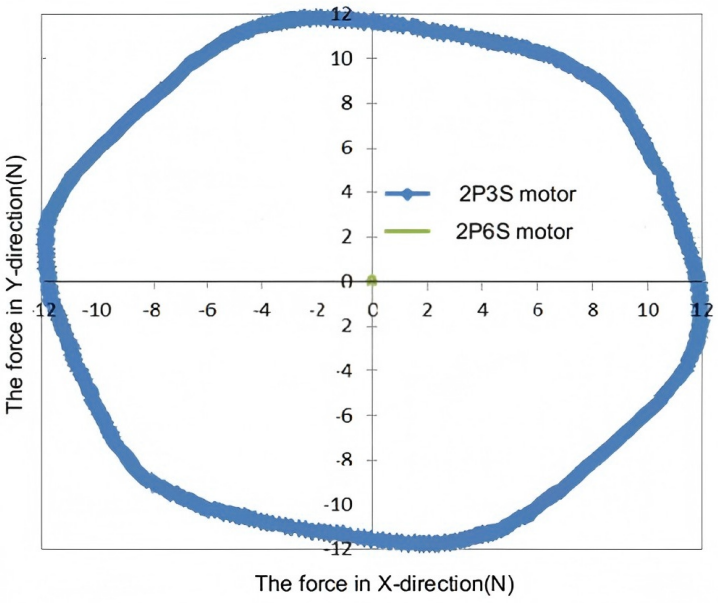

Figure 7. Comparison of periodic forces in-plane (X-Y direction) on the rotor within one revolution (2P6S vs. 2P3S motors).

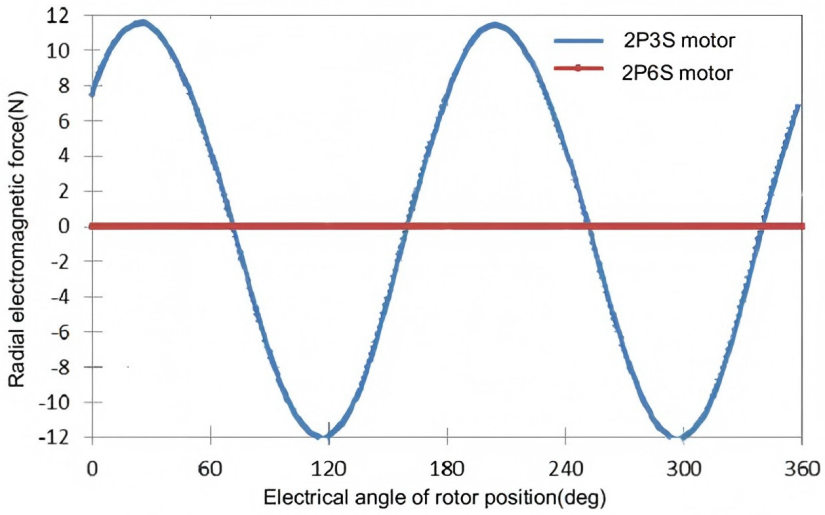

Figure 8. Comparison of radial forces between 2P6S and 2P3S motors.

The FEA results for the electromagnetic excitation forces of the two motors are compared, as shown in **Table 2**. Only the final results for torque ripple and cogging torque are listed. The 2P6S motor has a torque ripple of 32% and a cogging torque of 0.02 mN·m, both lower than the 40% and 0.05 mN·m of the 2P3S motor. Compared with the 2P3S design, the torque ripple and cogging torque of the 2P6S motor are reduced by 20% and 60%, respectively, although these improvements are not as pronounced as the elimination of the UMP. In other words, adopting the 2P6S design can improve the radial electromagnetic excitation, torque ripple, and cogging torque of the motor, especially by eliminating the radial unbalanced electromagnetic force.

Table 2. Comparison of electromagnetic excitation simulation results (2P3S vs. 2P6S).

Parameters	2P3S motor	2P6S motor
Rotor radial unbalanced force (N)	12	0
Electromagnetic torque ripple (%)	40	32
Cogging torque amplitude (mN·m)	0.05	0.02

The effect of radial UMP on the vibration noise of the motor is much greater than that of the torque ripple. This is because UMP is a radial force that directly acts on the rotor and bearings and is coupled with the stator. Torque ripple and cogging torque are caused by tangential forces, which do not directly excite other structural components. In the original 2P3S motor, the asymmetric magnetic circuit results in a severe UMP, with a single-sided peak of 12 N (equivalent to the force of a 1.2 kg mass on the rotor). Based on the improved pole-slot combinations and neglecting assembly errors, the 2P6S motor has no radial unbalanced force (UMP ≈ 0), which will effectively eliminate the 2f electromagnetic noise source.

3.2. Influence of segmented stator assembly gap

The variation of electromagnetic excitation under different assembly clearances (including vertical clearances and lateral offsets) is further analyzed using a 2P6S stator segmented structure, as shown in **Figure 9**.

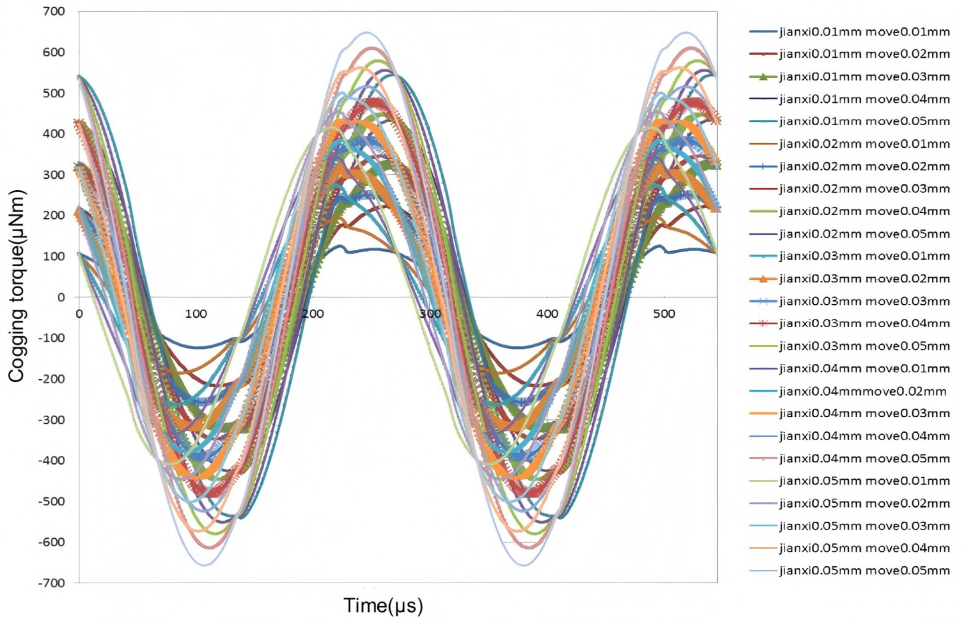

Figure 9. Cogging torque waveform during gap variation of stator components in a 2P6S motor.

Figure 9 shows the time-domain curves of the motor cogging torque when the vertical gap of the segmented stator changes from 0.01 mm to 0.05 mm and the lateral offset changes from 0.01 mm to 0.05 mm. The cogging torque of the 2P6S motor is highly sensitive to the assembly gap: when the gap is 0.01 mm, the cogging torque period changes from 6f to 2f, and the time-domain waveform has a significant 2f. The amplitude increases to about five times that of the ideal case without any gap,

where the cogging torque is about 100 μN·m. This indicates that the 2f component has become the main excitation. The Fourier analysis of cogging torque indicates there are higher-order frequency components in addition to the 2f frequency. However, the main focus remains the dominant 2f component.

Extracting the maximum cogging torque from each curve in **Figure 9** and plotting it against the stator vertical gap and lateral offset, the variation of cogging torque is obtained, as shown in **Table 3**. **Figures 10** and **11** show the cogging torque variation curves of the motor relative to lateral offset and vertical gap, respectively.

Table 3. Effect of the split stator vertical gap and lateral offset on cogging torque.

	Lateral offset (mm)						
	0.01	0.02	0.03	0.04	0.05		
Cogging torque (max. values, μN·m)	206.20	321.20	447.10	565.10	684.70	0.01	vertical gap (mm)
	369.60	421.30	525.30	637.50	749.30	0.02	
	543.90	580.60	644.70	723.60	829.90	0.03	
	721.50	748.80	799.10	864.20	940.40	0.04	
	902.90	924.10	964.40	1016.60	1082.10	0.05	

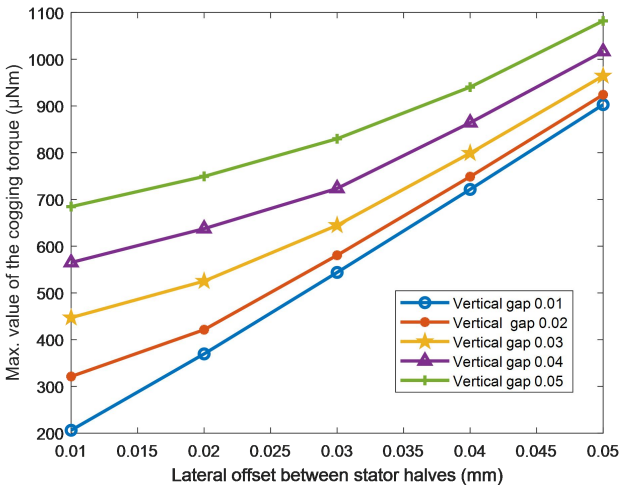

Figure 10. Variation of motor cogging torque with lateral offset between stator halves.

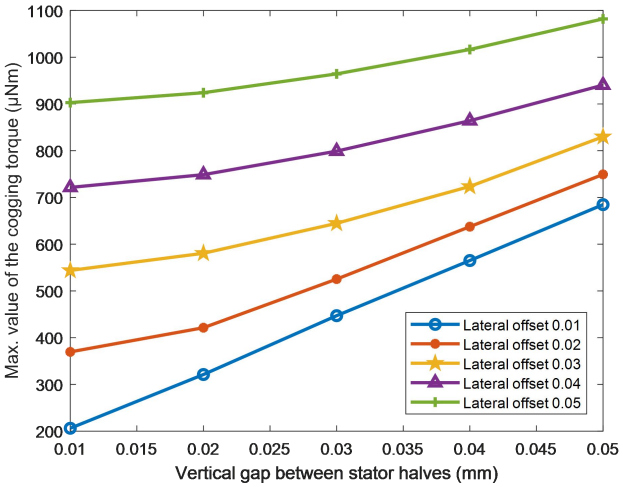

Figure 11. Variation of motor cogging torque with vertical gap between stator halves.

In **Figure 10**, for a given vertical gap, the cogging torque increases rapidly as the lateral offset increases. This sensitivity is especially significant when the vertical gap is small. For example, at a 0.01 mm vertical gap, increasing the lateral offset from 0.01 mm to 0.05 mm can increase the cogging torque from 206.2 μN·m to 902.9 μN·m (an increase of 696.7 μN·m, about 337%). At a 0.05 mm vertical gap, the cogging torque increases from 684.7 μN·m to 1082.1 μN·m (an increase of 397.4 μN·m, about 58%). These results indicate that compared with the 0.01 mm gap, the absolute and relative increase in cogging torque caused by offset are much smaller when the gap is 0.05 mm. In other words, a small vertical gap will generate a low absolute cogging torque, and this torque is highly sensitive to lateral offset (resulting in poor consistency between units). On the contrary, a larger vertical gap will lead to a higher cogging torque, which is less affected by offset (resulting in better consistency). Considering the practical machining tolerances and sample consistency, the vertical gap is limited to within 0.03 mm.

Similarly, **Figure 11** shows that for a given lateral offset, the cogging torque increases with the vertical gap, but the degree of increase is smaller than that when changing the lateral offset. In other words, the sensitivity of cogging torque to the vertical gap is slightly lower than its sensitivity to lateral offset. When the vertical gap is small, the change in the gap will lead to a significant change in cogging torque; once the gap reaches 0.05 mm, further increases in cogging torque will become smaller. **Figures 10** and **11** show that lateral offset and vertical gap will increase cogging torque, reducing the vibration and noise performance of the motor. To reduce the cogging torque of the motor, the segmented stator gap should be controlled. Considering manufacturing tolerances and production cost, both the vertical gap and lateral offset are limited to within 0.03 mm.

FEA is conducted on a motor with a vertical clearance of 0.03mm and a lateral offset of 0.03mm to calculate its radial electromagnetic excitation. **Figure 12** shows the time-frequency spectrum of the radial electromagnetic force at each stator tooth. Due to eccentricity, the 2P6S motor generates a UMP of spatial order 1 at 2f, with an amplitude of about 4.2 N. In other words, the stator assembly gap introduces 2f electromagnetic excitation in the motor. However, this amplitude is still much smaller than the 12 N electromagnetic force of the 2P3S motor, which is equivalent to a reduction of about 60% electromagnetic excitation force.

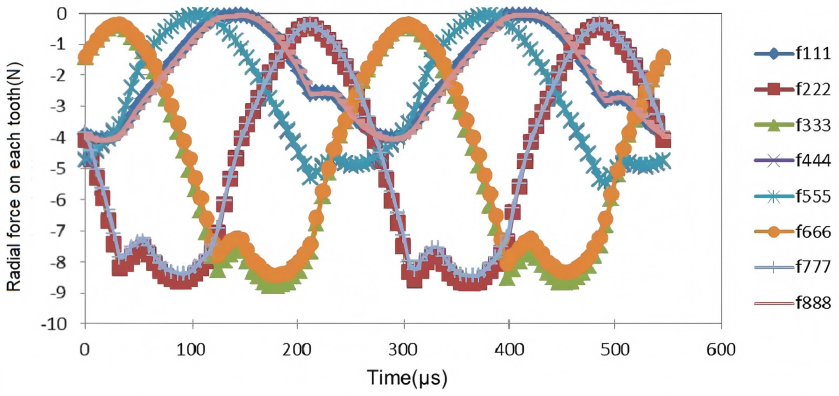

Figure 12. Radial electromagnetic force wave (time-frequency spectrum) at each stator tooth for the 2P6S motor with a 0.03 mm vertical gap and 0.03 mm lateral offset.

4. Experiment and results

Prototypes of the original and improved motor designs were constructed for noise tests. Three versions of the motor: (a) the original 2P3S design, (b) the improved 2P6S design with a stator assembly gap of about 0.03 mm (typical manufacturing tolerance), and (c) the improved 2P6S design with a reduced stator gap of about 0.01 mm (achieved through precision assembly), are evaluated. All prototypes were operated at the same speed of 120,000 rpm in the test. Noise measurements were carried out in a controlled environment using the LMS. Test Lab system. Four acoustic sensors (free-field microphones used as sound level meters) were placed around the motor to capture the radiated noise. Data acquisition and analysis are performed using LMS Test.Lab 2019.1 software. The measurement bandwidth ranged from 20 Hz to 10 kHz, including the relevant noise spectrum of the motor. To maintain consistency, the rotors of all prototypes have reached a high level of balance, so that any differences in noise could be mainly attributed to electromagnetic sources rather than mechanical unbalance.

Noise spectra for the original and improved motor prototypes are measured to evaluate how the simulated design translates into actual noise reduction. **Figure 13** shows the noise spectrum of the original 2P3S motor, with **Figure 13a** showing the narrow-band spectrum and **Figure 13b** showing the one-third-octave spectrum. The 2P3S motor shows significant tonal peaks at multiples of the rotational frequency (1f, 2f, 3f, etc.) atop a broadband noise floor. In the narrow-band plot, there is a significant peak at the 2f frequency, corresponding to twice the rotational speed (such as 4000 Hz at 120,000 rpm). The sound pressure level at the 2f frequency reaches about 77.3 dB(A) for the 2P3S motor, making it the highest single-frequency noise component. The component at the fundamental rotational frequency (1f) is around 71.2 dB(A), being also significant. According to the study by Feng et al. [13], the 1f noise in high-speed motors is usually attributed to rotor unbalance (mechanical eccentricity) and is often exacerbated by any aerodynamic excitation that also occurs with each revolution. In the test, despite careful balancing, the 1f noise remained above 70 dB(A), indicating there is some coupling of mechanical and aerodynamic sources at that frequency. The 2f noise in the 2P3S motor is mainly due to electromagnetic excitation, especially the force caused by UMP, as determined in the analysis. There is a strong 2f tone of about 77 dB(A) in the spectrum, which is consistent with the expected significant noise generated by the UMP induction force of the 2P3S motor. A peak at three times the rotational frequency (3f) is also evident, but at a lower level. This 3f component can be related to modulation effects: for example, an interaction between the 2f electromagnetic force and 1f mechanical vibration could generate a 3f response, or it may originate from certain slotting harmonics.

Figure 14 shows the noise spectrum of the improved 2P6S motor (with a stator gap of 0.03 mm). In these plots, **Figure 14a** shows the narrow-band spectrum and **Figure 14b** shows the one-third-octave spectrum. The 2f noise component is greatly reduced in the 2P6S motor. The highest tonal peak of the 2P6S is still at 2f, but its level is about 68.7 dB(A), lower than that of the 2P3S motor. The 1f noise of the 2P6S motor

is measured around 72 dB(A), slightly higher than the 1f noise of the 2P3S design in this test. The 3f noise component in the 2P6S motor remains evident, around 66 dB(A). This difference can be explained by the fact that both prototypes have balanced to a similar level; small differences in rotor balance or slight residual eccentricities can lead to similar 1f levels. It is expected that the 1f noise will not be significantly affected by the pole-slot modification, as 1f is mainly a mechanical phenomenon and the rotor mass balance remains unchanged. The slight increase in the 1f noise level (to 72 dB(A)) of the 2P6S motor may be due to a minor difference in rotor-stator eccentricity. For instance, a segmented stator with a 0.03 mm assembly gap may maintain slightly greater eccentricity than the one-piece stator of the 2P3S design.

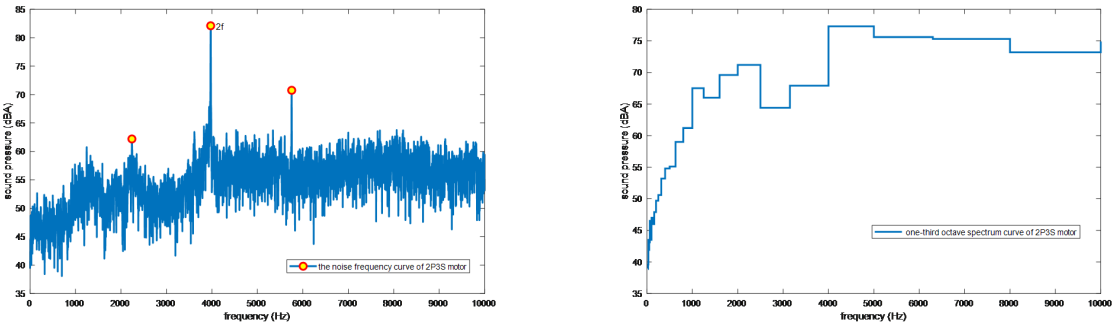

(**a**) (**b**)

Figure 13. Noise spectrum of the original 2P3S motor at 120,000 rpm; (**a**) narrow-band spectrum; (**b**) one-third-octave spectrum.

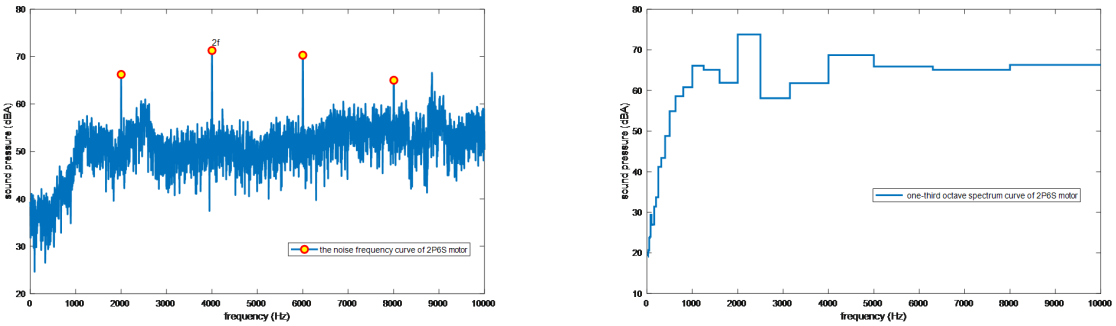

(**a**) (**b**)

Figure 14. Noise spectrum of the improved 2P6S motor at 120,000 rpm with 0.03 mm stator gap; (**a**) narrow-band spectrum; (**b**) one-third-octave spectrum.

To compare the noise profiles, **Figure 15** shows the one-third-octave noise spectra of the original 2P3S motor and the improved 2P6S motor. The noise of the 2P6S motor in the 2f band is much lower than that of the 2P3S motor, about 9 dB lower in the sound pressure level. This is significant because a 9 dB reduction is equivalent to approximately halving the perceived noise loudness to the human ear. This confirms that the pole-slot optimization has achieved a significant reduction in the primary electromagnetic noise. In addition, reducing 2f electromagnetic noise has another benefit: the 2P6S spectrum shows that some higher-frequency bands, such as around 3f, are also reduced to some extent. This is because reducing the main 2f excitation will also decrease inter-modulation products. These spectra confirm that the slot-pole

optimization effectively targets the dominant noise component and improves the overall acoustic signature of the motor. **Figure 16** compares the noise spectra of the improved 2P6S motor under two stator assembly gap conditions: the standard 0.03 mm gap and a reduced 0.01 mm gap. These spectra show that tightening the stator assembly gap yields further noise reduction at 2f. When the stator segment gap is reduced from 0.03 mm to 0.01 mm, the 2f noise level drops from about 68.7 dB(A) to 65.0 dB(A) (an improvement of about 3.7 dB). This is consistent with the simulation prediction that smaller gaps will reduce UMP, thereby reducing 2f noise. Compared with a 0.03 mm gap, the motor with a 0.01 mm gap shows a slight reduction in the 1f noise component. This can be explained by increasing concentricity: a smaller assembly gap makes the rotor more centered, and any rotor unbalance is low. In fact, the data shows that at a gap of 0.01 mm, the 1f noise is increased by about 1–2 dB. In the higher frequency range, reducing the assembly gap often reduces the noise at relevant excitation frequencies. For example, as the excitation of 2f and 1f decreases, the modulated component at 3f (the 2f ± 1f sideband) also decreases to some extent. Reducing the assembly gap from 0.03 mm to 0.01 mm will result in a decrease of nearly 4 dB in 2f noise. This confirms that strictly controlling the stator assembly gap is an effective measure to further improve the noise performance in the optimized design.

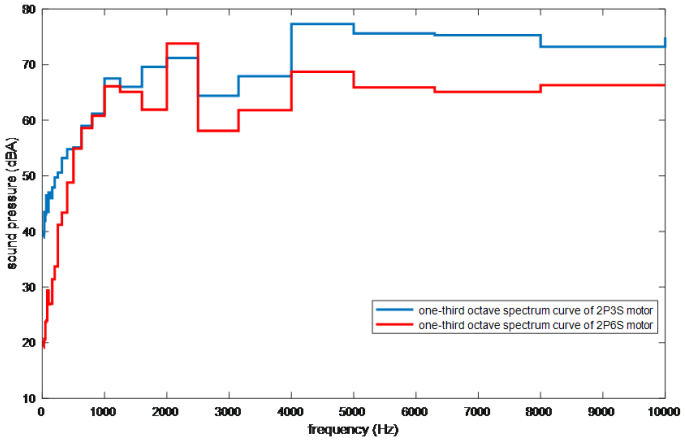

Figure 15. Comparison of one-third-octave noise spectra between the 2P3S and 2P6S motors.

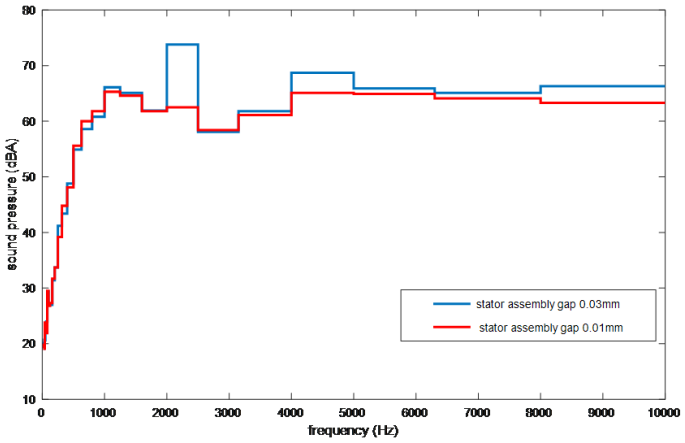

Figure 16. Noise spectra of the 2P6S motor under different stator assembly gap conditions (0.03 mm vs. 0.01 mm).

The experimental results validate the effectiveness of the proposed noise control strategies. The 2P6S pole-slot optimization greatly reduces the main 2f electromagnetic noise, and the segmented stator with a controlled gap provides additional noise attenuation under improved assembly precision. These findings indicate that a comprehensive approach is necessary. It should address electromagnetic noise at the source while minimizing assembly-induced disturbances, which can significantly improve the acoustic performance of ultra-high-speed motors.

5. Conclusion

The reduction of 2f electromagnetic noise in an ultra-high-speed permanent magnet synchronous motor (PMSM) was studied. Through theoretical analysis, the main excitation factors causing 2f noise were identified, and a comprehensive noise reduction scheme based on optimized pole slot combination and stator structure was proposed. The scheme was evaluated using finite element simulations and experimentally validated on a 120,000 rpm motor. The results indicate that the proposed measures can significantly lower the electromagnetic noise of the motor at 2f frequency, thereby improving the overall noise and vibration performance. The main findings are drawn as follows:

1) Optimizing the pole-slot combination from 2P3S to 2P6S can significantly reduce the 2f electromagnetic noise by eliminating UMP. Compared with 2P3S, the 2P6S design can completely eliminate UMP and reduce 2f noise by 9 dB. In addition, the 2P6S design can reduce the torque ripple by 20% and the cogging torque by 60%. These results highlight the effectiveness of pole-slot optimization in reducing noise and improving motor performance.
2) Controlling the stator assembly gap is essential for minimizing additional low-order radial force waves that exacerbate 2f noise. Misalignments or gaps larger than 0.01 mm can increase 2f electromagnetic forces and reintroduce UMP. When maintaining strict tolerances (with both lateral offset and vertical clearance below 0.03mm), UMP is significantly reduced, resulting in a 60% decrease in 2f force. These findings indicate the crucial role of precision in reducing noise during stator assembly of ultra-high-speed motors.
3) Both simulations and experiments validate the effectiveness of the combined pole-slot optimization and stator assembly gap control in reducing 2f noise. Experimental tests have shown that compared with 2P3S, the 2f noise of the 2P6S design has been reduced by 9 dB. Further noise reduction (3.7 dB) is achieved by reducing the stator gap from 0.03 mm to 0.01 mm. There is also a reduction in 3f and 1f noise, supporting the comprehensive effectiveness of the proposed noise reduction strategies.

Future research will explore the applicability of the proposed methods to motors with higher pole counts, such as 2P9S, 4P6S, and others, where the 2f frequency will shift to higher values, potentially affecting excitation responses. A systematic study is needed to evaluate the performance of these methods in motors with higher speeds and different pole configurations. The research will focus on understanding the

coupling between electromagnetic, mechanical, and aerodynamic forces at high speeds, where aerodynamic effects become more significant in noise generation. Further work will also address the scalability and precision of manufacturing processes to ensure consistent performance in mass production.

Author contributions: study conception and design: GF, RJ; Methodology: RJ; Validation: JY, JZ; Simulation: GF, RJ; resources: JZ; data curation: JY; writing-original draft preparation, GF; writing-review and editing, WZ, DL. All authors reviewed the results and approved the final version of the manuscript.

Funding: This research was funded by the Start-up Fund for New Ph.D. Researchers of Suzhou Chien-Shiung Institute of Technology (2025), Funding Program of State Key Laboratory of Intelligent Optimized Manufacturing in Mining & Metallurgy Process (Grant No. BGRIMM-KZSKL-2024-21), and Qing Lan Project of Jiangsu Province (2025).

Institutional review board statement: Not applicable.

Informed consent statement: Not applicable.

Data availability statement: The data used to support the findings of this study are available from the corresponding authors upon request.

Acknowledgment: The authors would like to acknowledge the support from the Start-up Fund for New Ph.D. Researchers of Suzhou Chien-Shiung Institute of Technology (2025), Funding Program of State Key Laboratory of Intelligent Optimized Manufacturing in Mining & Metallurgy Process, and Qing Lan Project of Jiangsu Province (2025).

Conflict of interest: The authors declare no conflict of interest.

References

1. Gao QX, Wang XL, Zhang Y. Multi-physical-field characteristics modeling and structure optimization for kW-level ultra-high speed PM motors with integrated support system. Chinese Journal of Aeronautics. 2023; 36(4): 455–467.
2. Wang DH, Xu S, Li Y, et al. Sensorless control impact on electromagnetic vibrations and acoustic noises in interior permanent magnet synchronous machines. IEEE Transactions on Transportation Electrification. 2024; 11(1): 416–425.
3. Liu CC, Zhang HM, Wang SH, et al. Multiphysical design and optimization of High-Speed Permanent Magnet Synchronous Motor with sinusoidal segmented permanent magnet structure. Journal of Electrical Engineering & Technology. 2023; 19: 1459–1473.
4. Peng C, He JX, Zhu MT, et al. Optimal synchronous vibration control for magnetically suspended centrifugal compressor. Mechanical Systems and Signal Processing. 2019; 132: 776–789.
5. Yi FY, Su QQ, Feng CX, et al. Response analysis and stator optimization of Ultrahigh-Speed PMSM for fuel cell electric air compressor. IEEE Transactions on Transportation Electrification. 2023; 9: 5098–5110.
6. Bianchi N, Bolognani S, Pré M. Design techniques for reducing the cogging torque in surface-mounted PM motors. IEEE Transactions on Industry Applications. 2002; 38(5): 1259–1265.
7. Zhu ZQ, Howe D. Influence of design parameters on cogging torque in permanent magnet machines. IEEE Transactions on Energy Conversion. 2000; 15(4): 407–412.
8. Jahns TM, Soong WL. Pulsating torque minimization techniques for permanent magnet AC motor drives—A review. IEEE Transactions on Industrial Electronics. 1996; 43(2): 321–330.

9. Islam MS, Mir S, Sebastian T. Issues in reducing the cogging torque of mass-produced permanent-magnet brushless DC motor. In: Proceedings of the 38th IAS Annual Meeting on Conference Record of the Industry Applications Conference; 12–16 October 2003; Salt Lake City, UT, USA. pp. 1356–1363.
10. Wang A, Jia Y, Soong WL. Comparison of five topologies for an interior permanent-magnet machine for a hybrid electric vehicle. IEEE Transactions on Magnetics. 2011; 47(10): 3606–3609.
11. Anuja TA, Doss MAN. Reduction of cogging torque in surface mounted permanent magnet brushless DC motor by adapting rotor magnetic displacement. Energies. 2021; 14(10): 2861.
12. Huang PC, Ma JE, Zheng GL, et al. Characteristic analysis and control study of aerodynamic noise in Self-Ventilated traction motors. Electric Machines & Control Application. 2024; 51(10): 1–7. (in Chinese).
13. Feng GP, Zhou WJ, Li DY, et al. Analysis and Control of Rotating Frequency Noise Induced by High-speed Rotation of Fan Machines. Noise and Vibration Control. 2024; 44(6): 309–314. (in Chinese).
14. Jamali Arand S, Ardebili M. Cogging torque reduction in axial-flux permanent magnet wind generators with yokeless and segmented armature by radially segmented and peripherally shifted magnet pieces. Renewable Energy. 2016; 99: 95–106.
15. Ilka R, Alinejad-Beromi Y, Yaghobi H. Cogging torque reduction of permanent magnet synchronous motor using multi-objective optimization. Mathematics and Computers in Simulation. 2018; 153: 83–95.
16. Lin F, Zuo SG, Deng WZ, et al. Reduction of vibration and acoustic noise in permanent magnet synchronous motor by optimizing magnetic forces. Journal of Sound and Vibration. 2018; 429: 193–205.
17. Wang SM, Hong JF, Sun YG, et al. Analysis of Zeroth Mode Slot Frequency Vibration of Integer Slot Permanent Magnet Synchronous Motors. IEEE Transactions on Industrial Electronics. 2019; 67(4): 2954–2964.
18. Yang ZG, Li W, Gou YN, et al. Research on Radial Force of Permanent Magnet Synchronous Motor Based on Maxwell. Journal of Electrical Engineering & Technology. 2020; 15: 2601–2608.
19. Ge HR, Qiu X, Guo BC, et al. Optimized Rotor Shape for Reducing Torque Ripple and Electromagnetic Noise. IEEE Transactions on Magnetics. 2021; 58(2): 8102905.
20. Wu ZP, Zuo SG, Huang ZY, et al. Modelling, calculation and analysis of electromagnetic force and vibroacoustic behavior of integer-slot permanent magnet synchronous motor considering current harmonics. Journal of Vibration Engineering & Technologies. 2022; 10: 1135–1152.
21. Chen Y, Zhu ZQ, Howe D. Vibration of PM brushless machines having a fractional number of slots per pole. In: Proceedings of the 2006 IEEE International Magnetics Conference (INTERMAG); 8–12 May 2006; San Diego, CA, USA.
22. Petkovska L, Lefley P, Cvetkovski LV. Design techniques for cogging torque reduction in a fractional-slot PMBLDC motor. COMPEL. 2020; 39(5): 1041–1055.
23. Zhou JY, Xiao X. Combined methods for torque variation reduction of high-speed FSPM. Energy Reports. 2023; 9(8): 199–206.
24. Xing ZZ, Wang XH, Zhao WL. Optimization of stator slot parameters for electromagnetic vibration reduction of permanent magnet synchronous motors. IEEE Transactions on Transportation Electrification. 2022; 8(4): 4337–4347.
25. Wang XQ, Wu M, Zhao PP. Dielectric identification method and system design of coal gangue based on frequency shift characteristics. Scientific Reports. 2025; 15: 8712.
26. Chen YY, Xiao Y, Ji C, et al. An Online Torque Prediction Method of PMSM Using PINNs. IEEE Access. 2025; 13: 196796–196808.
27. Feng GP, Chen Y, Huang XC, et al. Study on transmission paths in submarine stern excited longitudinally. Noise and Vibration Control. 2009; 29(6): 132–135. (in Chinese).
28. Zhu ZQ, Ishak D, Howe D, et al. Unbalanced magnetic forces in permanent-magnet brushless machines with diametrically asymmetric phase windings. IEEE Transactions on Industry Applications. 2007; 43(6): 1544–1553.
29. Chen YX, Zhu ZQ, Ying SC. Electric Machine Noise Analysis and Control. Zhejiang University Press; 1987. (in Chinese).